OPTICAL EFFECTS ON THE CHARACTERISTICS OF A NANOSCALE FINFET

R. Ramesh

Department of Electronics and Communication Engineering
M.A.M College of Engineering
Trichy-621 105, TamilNadu, India

M. Madheswaran

Center for Advanced Research
Muthayammal Engineering College
Rasipuram, TamilNadu, India

K. Kannan

Department of Mathematics
SASTRA University
Thanjavur, TamilNadu, India

Abstract—The effect of optical radiation on a uniformly doped nanoscale FinFET considering quantum mechanical effects has been theoretically examined and analyzed. The device characteristics are obtained from the self-consistent solution of 3D Poisson-Schrödinger equation using interpolating wavelet method. To our best knowledge this is the first approach for the self-consistent solution to surface potential computations of nanoscale FinFET photodetector using interpolating wavelets. This method provides more accurate results by dynamically adjusting the computational mesh and scales the CPU time linearly with the number of mesh points using polynomial interpolation, hence reducing the numerical cost. A fine mesh can be used in domains where the unknown quantities are varying rapidly and a coarse mesh can be used where the unknowns are varying slowly. The results obtained for dark and illuminated conditions are used to examine the performance of the device for its suitable use as a photodetector.

Corresponding author: R. Ramesh (ramesh24.dr@gmail.com).

1. INTRODUCTION

The photosensitivity and integrated circuit compatibility of Field-Effect Transistors (FETs) have extended the potential of these devices for their use as photodetectors. Among the FETs configuration, Metal Semiconductor Field Effect Transistor (MESFET) and High Electron Mobility Transistor (HEMT) have been studied theoretically as well as experimentally by several researchers for various optically-controlled applications [1–5]. A three dimensional modeling of a nano MISFET photodetector without including quantum mechanical effects [6] has been reported. A transition from bulk to multiple-gate fully depleted (FD) silicon-on-insulator (SOI) offers drive current and better short-channel immunity [7]. CMOS designs below 0.1 μm are severely constrained by short channel effects (SCE) and gate insulator tunneling [8–11]. One of the approaches to circumvent the gate tunneling restriction is to change the device structure so that the MOSFET gate length can be further scaled even with thicker oxide. Double-gate MOSFET (DGFET) is one of the most promising devices for channel length in the range 10–30 nm [12–15]. The alignment of the top and bottom gates to each other and to source/drain (S/D) doping is crucial to device performance, because misalignment may cause extra gate-to-S/D overlap capacitance as well as S/D series resistance [16]. In order to optimize the performance of double gate devices, self-aligned processes and structures are proposed, with FinFET being one of the most promising [17–21]. The FinFET is a symmetric three-gate structure, hence requires 3-D analysis. The variation in the channel potential of FinFET with doped and undoped channels has been reported [22]. The 3-D analytical modeling of FinFET by solving the Poisson's equation has also been reported [23–25]. The existing literatures reported on analytical modeling have shown the complexity in evaluating various device characteristics including QM effects. In addition, it has been found that many assumptions and approximations have to be incorporated while the device is analytically modeled. In FinFET devices, quantum effects and non-equilibrium, ballistic or near-ballistic transport have great impact on device performance [26]. The carriers transport ballistically if the channel length is comparable to the carrier scattering length [27]. An analytical charge model based on self-consistent solution of Poisson's and Schrödinger equation for 3-D FinFETs is carried out [28]. A ballistic quantum-mechanical simulation using CBR (Contact Block Reduction) method to investigate the behavior of 10 nm FinFET device is reported [29]. Double-gate FinFET devices with symmetric and asymmetric poly-silicon gates have been fabricated [30].

FinFET is developed with special emphasis on process simplicity and compatibility with conventional CMOS technology [31]. A simple capacitive model was proposed by [32] to predict the relationship between Drain Induced Barrier Lowering (DIBL) and subthreshold swing. Ben Abdallah proposed the modeling of ballistic quantum transport in nanostructures using the decomposition of the wave function with reduced simulation time [33]. A numerical scheme for the 1-D Schrödinger equation used to simulate a resonant tunneling diode uses the oscillating interpolating function from WKB (Wentzel Kramers Brillouin) asymptotic [34]. But this method provides less accurate results since it incorporates 1-D Schrödinger equation. A 3-D quantum simulation of silicon nanowire transistors with the effective mass approximation using mode space approach producing high computational efficiency is proposed [35]. A numerical solution of coupled Poisson-Schrödinger equation for device modeling of nanoscale FinFET using Newton's method has been reported [36].

In recent years, modeling and simulation of devices has been carried out by means of new mathematical tools, such as the wavelet method [37]. A solution for 2D simulation of a pn-diode without including quantum mechanical effects has been obtained. Wavelet coefficients have been used in time-varying problems [38], but this approach computes the solution on a uniform grid at the finest resolution [39]. On the other hand, implementing a technique that adaptively refines the mesh in domains where the unknown quantities vary rapidly would considerably reduce the number of unknowns. The wavelet method uses such a technique and corresponds to a multiresolution analysis of a problem. It was demonstrated [40] that finite-difference scheme can be derived by wavelet expansions. The resulting numerical technique is called multiresolution time-domain technique (MRTD) [41]. This method shows very good performance as for the accuracy, memory requirements and CPU time. The MRTD can be regarded as a wavelet-based Galerkin method. For nonlinear equations used for semiconductor device modeling, this method can become quite time consuming. A 2D simulation of MESFET using Poisson's equation and current continuity equations is performed using a non-uniform mesh generated by interpolating wavelet scheme [42]. Hussein et al. proposed a time-domain approach to solve the hydrodynamic model for the simulation of devices using self-adaptive grids [43]. They have implemented only the Poisson's equation and current continuity equation for their model. Toupikov et al. proposed a nonlinear modeling of semiconductor devices by solving 2D Poisson's equation using sparse point representation based on interpolating wavelets [44]. All the above literatures did not include

the quantum mechanical effects for obtaining a self-consistent solution using wavelets.

In this paper, a self-consistent solution for 3D numerical model of nanoscale FinFET photodetector including QME using interpolating wavelets has been developed and presented. The prime focus is to obtain the device characteristics under illumination, by numerically solving the 3D Poisson-Schrödinger equations directly until self-consistency is achieved. The 3-D simulation is necessary to describe the 3-D characteristics of FinFETs structure. The direct solution of 3D Poisson-Schrödinger equation provides more accurate results than the WKB approximation. The finite element (FE) or finite difference (FD) methods require a large number of grid points for obtaining self-consistent solution of 3D Poisson-Schrödinger equation thus unnecessarily increasing the numerical cost. The interpolating wavelet method reduces the numerical cost of the simulation further and produces more accurate results with much coarser grids. It provides a very good performance in terms of CPU time savings and fast convergence.
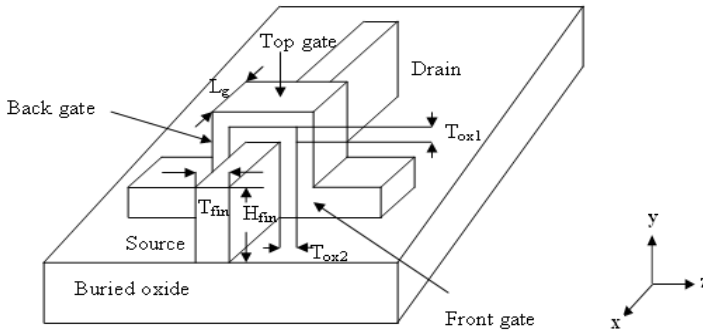

Figure 1. Schematic diagram of FinFET.

2. PHYSICS BASED MODELING

The general FinFETs structure is shown in Fig. 1 [25]. The following are the geometrical parameters.

i) Gate Length (L_g): The physical gate length of FinFETs, defined by spacer gap.

ii) Fin Height (H_{fin}): The height of silicon fin, defined by the distance between the top gate and buried oxide layer (BOX).

iii) Fin Width (T_{fin}): The thickness of silicon fin, defined between the front and back gates.

iv) Top gate thickness (T_{ox1}): The thickness of the top gate oxide.

v) Front or back gate thickness (T_{ox2}): The thickness of the front or back gate oxide.

vi) Channel Length (L_{eff}): The channel length is estimated by the metallurgical junction for abrupt junctions.

Geometrical channel width is defined as $W = 2 \times H_{fin} + T_{fin}$.

When T_{fin} is much larger than H_{fin} or when top gate oxide is much thinner than the front and back oxides, FinFET can be treated as single-gate fully depleted SOI MOSFET (FDFET) as long as the silicon fin remains fully depleted [23]. When H_{fin} is much larger than T_{fin} or top gate oxide (T_{ox1}) is much thicker than the front and back oxides (T_{ox2}), FinFET can be treated as DGFET [23]. It is difficult to assume a simple potential distribution because of its asymmetric 3-D structure. The electrostatic potential in the subthreshold region can be described by the 3-D Poisson's equation.

$$\frac{\partial^2 U(x,y,z)}{\partial x^2} + \frac{\partial^2 U(x,y,z)}{\partial y^2} + \frac{\partial^2 U(x,y,z)}{\partial z^2}$$
$$= \frac{q[N_a(x,y,z) - n(x,y,z) + p(x,y,z)]}{\varepsilon_s} + \Delta n \qquad (1)$$

where $U(x,y,z)$ is the surface potential at a particular point (x,y,z), and $N_a(x,y,z)$ is the uniform channel doping concentration. q is the electronic charge, and ε_s is the permittivity of silicon. $n(x,y,z)$ is the electron concentration, and $p(x,y,z)$ is the hole concentration. Δn is the excess carriers generated per unit volume. The boundary conditions are

$$U\big|_{y=H_{eff}} = V_g - V_{fb}. \qquad\qquad U\big|_{z=-T_{eff}/2} = V_g - V_{fb}.$$

$$U\big|_{z=T_{eff}/2} = V_g - V_{fb}. \qquad\qquad U\big|_{x=0} = V_{bi} + V_{op}$$

$$U\big|_{x=L_{eff}} = V_{bi} + V_{ds} + V_{op} \qquad U\big|_{y=-H_{eff}} = V_g - V_{fb}.$$

The electron concentration can be obtained from

$$n(x,y,z) = \sum_{j=1}^{3} \sum_{i=1}^{\infty} n_{ij} |\psi(x,y,z)|^2 \qquad (2)$$

where j is the valley and i is the subband.

$$n_{ij} = \frac{n_{vj} m_{dj} k_B T}{\pi \hbar^2} \ln\left[1 + \exp\left(\frac{E_{Fn} - E_{ij}}{k_B T}\right)\right] \qquad (3)$$

where (3) expresses the number of electrons occupying the ijth electron energy level. m_{dj} is the electron density-of-states mass, and n_{vj} is the valley degeneracy. E_{fn} is the electron quasi-Fermi level, and E_{ij} is the electron energy states and explained in [49]. The Fermi-Dirac distribution at the source and drain ends are given in [26].

The excess carriers generated per unit volume due to the absorption of incident optical power density are given by [6]

$$\Delta n = \frac{1}{W_m} \int_0^{W_m} G_{op}(x)\,\tau_L dy \tag{4}$$

where W_m is the maximum width of the depletion layer and given by

$$W_m = [4\varepsilon_s \ln(N_a/n_i)/q\beta N_a]^{1/2} \tag{5}$$

where N_a is the acceptor concentration. $G_{op}(x)$ is the excess carrier generation rate at any point x in the semiconductor and is given by

$$G_{op}(x) = \frac{p_{opt}}{h\gamma}\,(1 - R_m)\,(1 - R_i)\,(1 - R_s)\,\alpha e^{-\alpha y} \tag{6}$$

where P_{opt} is the incident optical power density, and h is the Planck's constant. γ is the operating frequency, and α is the absorption coefficient of the semiconductor at the operating wavelength. R_m, R_i and R_s are the reflection coefficient at the metal gate entrance, gate-insulator interface and insulator-semiconductor interface respectively.

3. MULTIRESOLUTION ANALYSIS AND WAVELETS

For semiconductor device simulation using partial differential equations, the grid generation is very important. Grid points must be present accurately approximate to any physical quantity to be measured. The grid layout should be chosen carefully since the computational cost grows with the number of grid points. The difficulty in semiconductor device simulation is due to the different mesh sizes between substrate and doped regions. Finer mesh is needed in doped regions and junctions and coarse mesh for substrate regions, to reduce the number of unknowns and also the simulation time. Hence wavelets with MRA concept are used to achieve this goal. The Wavelet-Galerkin method uses the finite difference method with grid refinement. So, instead of letting the magnitude of wavelet coefficients choose the basis function in Galerkin approach, let the same coefficients choose grid points [45].

MRA is an important concept in wavelet theory. Many useful orthonormal wavelets are constructed within this framework. In

order to give a good explanation of the relationship between MRA and wavelet basis, a brief summary of Daubechies wavelets are given [46, 47]. The usefulness of wavelets for solving partial differential equations relies on the definition of MRA. An MRA is based on two fundamental concepts: nested subspaces and orthonormal bases. The first decomposes information into different scales; the second allows stable and fast algorithms. The space of square integral functions on the real line is denoted by $L^2(R)$. The orthonormal basis of wavelets of $L^2(R)$ is formed by dilations and translations of a single function $\Psi(x)$, called a mother wavelet.

$$\Psi_{jk}(x) = 2^{j/2}\Psi(2^j x - k), \quad j, k \in \mathbb{Z}. \tag{7}$$

The function $\Psi(x)$ has a companion, the scaling function $\varphi(x)$. They both satisfy the following two-scale relation

$$\varphi(x) = \sum_k a_k \varphi(2x - k), \tag{8}$$

$$\Psi(x) = \sum_k (-1)^k a_{1-k} \varphi(2x - k), \tag{9}$$

where the coefficients $a_k (k = 0, 1, \ldots, L-1)$ appearing in the two-scale relations (8) and (9) are called the wavelet filter coefficients. The support of the scaling function φ is the interval $[0, L-1]$ while that of the corresponding wavelet Ψ is the interval $[1 - L/2, L/2]$. The Daubechies wavelet filter coefficients for $L = 4, 6, 8, 10$ are listed in [23]. The theory for Interpolating wavelets can be found in [42, 44, 45].

The 3D effective mass Schrödinger equation along the n-channel is given by [26]

$$-\left[\frac{\hbar^2}{2m_x^*}\frac{\partial^2}{\partial x^2} + \frac{\hbar^2}{2m_y^*}\frac{\partial^2}{\partial y^2} + \frac{\hbar^2}{2m_z^*}\frac{\partial^2}{\partial z^2} + qU_{(x,y,z)}\right]\psi_{x,y,z} = E\psi_{x,y,z} \tag{10}$$

In the above equation, m_x^*, m_y^*, m_z^* are effective masses in the x, y and z directions.

$m_x^* = m_l = 0.916m_0, m_y^* = m_t = 0.19m_0, m_z^* = m_t = 0.19m_0$. E is the eigen energy, and $\hbar$ is the reduced Planck's constant. q is the charge of an electron. $U(x, y, z)$ is the surface potential, and $\psi(x, y, z)$ is the eigen wave function. The mixed Dirichlet and von Neumann boundary conditions were used for solving the 3-D Schrödinger equation because the Dirichlet boundary conditions force density of electrons to decrease to zero at contacts while density increases under von Neumann boundary conditions. For these reasons, the 3-D Schrödinger equation is solved using Dirichlet and von Neumann boundary conditions and normalized the states to 1/2. The

mixed Dirichlet and von Neumann boundary conditions are given by

$$\int |\psi_n(z)|^2 dz = 1/2 \tag{11}$$

This means that a constant function is obtained by summing the cosine functions from Dirichlet boundary conditions and the sine functions from von Neumann boundary conditions with normalization to 1/2. By solving the Schrödinger equation, the quantized states that are occupied by local quasi-Fermi levels were obtained.

In this section, the direct solution of 3-D Schrödinger equation (10) with mixed Dirichlet and Von Neumann boundary conditions is obtained using wavelet method. The wavelet approximation to the solution $\psi_j(x, y, z)$ at scale j is

$$\psi_j(x, y, z) = \sum_k \sum_l \sum_m \tilde{c}_{k,l,m} 2^{j/2}$$
$$\varphi(2^j x - k) 2^{j/2} \varphi\left(2^j y - l\right) 2^{j/2} \varphi\left(2^j z - m\right) \quad k, l, m \in Z \tag{12}$$

where $\tilde{c}_{k,l,m}$ are the wavelet coefficients, i.e., they define the solution in wavelet space.

Equation (12) can be simplified to

$$\sum_k \sum_l \sum_m \tilde{c}_{k,l,m} \varphi_{jk}(x) \varphi_{jl}(y) \varphi_{jm}(z) \tag{13}$$

where

$$\varphi_{jk}(x) = 2^{j/2} \varphi_{jk}(2^j x - k), \quad \varphi_{jl}(y) = 2^{j/2} \varphi_{jl}(2^j y - l),$$
$$\varphi_{jm}(z) = 2^{j/2} \varphi_{jm}(2^j z - m), \quad j > 0,$$

$k, l, m = 2 - N, 3 - N, \ldots, 2^j - 1$ are $2^j + N - 2$ unknown coefficients. j fixes the level of resolution. The larger the value of j is, the more accurate a solution can be obtained. But the number of equations required to solve the unknown coefficients is increased. In Equation (13), the parameter N represents the wavelet associated with the set of N Daubechies filter coefficients used as the solution bases. Substituting the wavelet series approximation $\psi_j(x, y, z)$ in Equation (13) for $\psi(x, y, z)$ yields [48]

$$\sum_k \sum_l \sum_m \tilde{c}_{k,l,m} \left(-\frac{\hbar}{2m_x^*} \frac{d^2}{dx^2} \varphi_{jk}(x) - \frac{\hbar}{2m_y^*} \frac{d^2}{dy^2} \varphi_{jk}(y) \right.$$
$$\left. -\frac{\hbar}{2m_z^*} \frac{d^2}{dz^2} \varphi_{jk}(z) + (qU_{x,y,z} - E)\varphi_{jk}(x)\varphi_{jl}(y)\varphi_{jm}(z) = 0 \right) \tag{14}$$

To determine the coefficient $c_{k,l,m}$, we take the inner product of both sides of Equation (14) with φ_{jn}

$$\sum_k \sum_l \sum_m \tilde{c}_{k,l,m} \left(-\frac{\hbar^2}{2m_x^*} \right) \int_0^{L_{eff}} \varphi_{jk}''(x)\varphi_{jn}(x)$$

$$-\frac{\hbar^2}{2m_y^*} \int_0^{H_{eff}} \varphi_{jl}''(y)\varphi_{jn}(y) - \frac{\hbar^2}{2m_z^*} \int_0^{T_{eff}} \varphi_{jm}''(z)\varphi_{jn}(z)$$

$$+(qU_{x,y,z} - E)\varphi_{jk}(x)\varphi_{jl}(y)\varphi_{jm}(z) = 0$$

$$\text{for } n = 2 - N, 3 - N, \ldots, 2^j - 1 \qquad (15)$$

where prime $'$ denotes differentiation with respect to the indicated independent variable. L_{eff} is the length of the channel, and H_{eff} is the height of the fin. T_{eff} is the thickness of the fin.

For simplicity, we define the following notations for integrals appearing in (15)

$$a_{kn}^j = \int_0^{L_{eff}} \varphi_{jk}''(x)\varphi_{jn}(x)dx = 2^{2j}[\Gamma_{k-n}^2(2^j - n) - \Gamma_{k-n}^2(-n)], \quad (16)$$

$$b_{kn}^j = \int_0^{H_{eff}} \varphi_{jl}''(y)\varphi_{jn}(y)dy = 2^{2j}[\Gamma_{l-n}^2(2^j - n) - \Gamma_{l-n}^2(-n)], \quad (17)$$

$$c_{kn}^j = \int_0^{T_{eff}} \varphi_{jm}''(z)\varphi_{jn}(z)dz = 2^{2j}[\Gamma_{m-n}^2(2^j - n) - \Gamma_{m-n}^2(-n)], (18)$$

and

$$d_{kn}^j = \int_0^{L_{eff}} \int_0^{H_{eff}} \int_0^{T_{eff}} \varphi_{jk}(x)\varphi_{jn}(x)\varphi_{jk}(y)\varphi_{jn}(y)\varphi_{jk}(z)\varphi_{jn}(z)dxdydz$$

$$= \Gamma_{k-n}^0(2^j - n) - \Gamma_{k-n}^0(-n)], \qquad (19)$$

Using the notations defined in Equations (16)–(19) we write Equation (15) as

$$\sum_k \sum_l \sum_m \tilde{c}_{k,l,m} \left(a_{kn}^j + b_{kn}^j + (qU_{x,y,z} - E)\, c_{kn}^j \right) = 0;$$

$$n = 2 - N, 3 - N, \ldots, 2^j - 1 \qquad (20)$$

The above Equation (20) can be put into the matrix-vector form

$$A\psi + B\psi + h(x, y, z)C = 0 \tag{21}$$

where

$$A = [a^j_{kn}]_{2-N \leq k,n \leq 2^j-1}, \quad B = [b^j_{kn}]_{2-N \leq k,n \leq 2^j-1},$$
$$\psi = [\psi_{j,2-L}, \psi_{j,3-L}, \ldots, \psi_{j,2^j-1}]^\tau, \quad C = [c^j_{kn}]_{2-N \leq k,n \leq 2^j-1}$$
$$\psi^2 = [\psi^2_{j,2-L}, \psi^2_{j,3-L}, \ldots, \psi^2_{j,2^j-L}]^\tau,$$

where τ denotes the transpose matrix.

Equation (21) can be written as

$$A_1\psi_{i+1} - A_2\psi_i + A_1\psi_{i-1} \tag{22}$$

This system may be easily solved by variety of methods. In this paper, we have used Cholesky's decomposition method. By solving this system, we obtain an accurate solution at resolution level j. We can calculate the absolute error defined as:

$$\text{Absolute error} = |\psi_{\text{exactsolution}} - \psi_{\text{Wavelet}}|$$

The drain current I_D considering scattering effects is given by [25, 27]

$$I_D = \frac{Wqn_i(V_{gs} - V_T)\left(1 - \exp\left(-\frac{V_{ds}}{V_T}\right)\right)}{\left[\frac{1}{v_T} + \frac{1}{D_{eff}/\ell}\right] \int\limits_0^{L_{eff}} \frac{dx}{\int\limits_{-H_{fin}/2}^{H_{fin}/2} \int\limits_{-T_{fin}/2}^{T_{fin}/2} \exp\left[\frac{U(x,y,z)}{V_T}\right] dy dz}} \tag{23}$$

where $v_T = \sqrt{2K_BT/\pi m^*}$ is the thermal velocity independent of the Fermi level. $D_{eff} = (K_BT/q)\mu_{eff}$ is the diffusion coefficient. For low V_{ds}, the critical length $\ell \rightarrow L$, the channel length. Assuming that only the lowest side band is occupied, the effective mass is $m* = m_t = 0.19m_0$ which gives a thermal velocity $v_T = 1.2 \times 10^7$ cm/s. By Mathiessen's rule $\mu_{eff}^{-1} = \mu_0^{-1} + \mu_B^{-1}$ where $\mu_B = \frac{qL}{m*\pi v_T}$ is the ballistic mobility, and $\mu_B = \frac{qL}{m*\pi v_T}$ is the low field mobility. λ is the mean free path, and $W = T_{fin}$ is the width of the device.

The subthreshold swing S is a measure of the gate control on the channel. It can be expressed as

$$S = \frac{\partial V_{gs}}{\partial \log I_{DS}}$$
$$S = \frac{\ln 10}{\beta} \times \frac{1}{1 - 2\Gamma_{11}e^{-\alpha} \times \sin\frac{\pi(x_c+a+c)}{a_{eff}} \times \sin\frac{\pi(y_c+b+d)}{b_{eff}}} \tag{24}$$

In which β and α are defined in [25]. x_c and y_c describe the position of the leakage path in the fin cross section. x_c could be set to zero due to symmetry, while y_c is determined by the geometrical features, doping concentration, and applied voltages.

4. COMPUTATIONAL TECHNIQUE

The 3D Poisson's equation (1) using the boundary conditions is solved numerically using Leibmann's iteration method to determine the approximate surface potential for a fixed value of gate voltage and assumed value of drain voltage. This value of surface potential is given to the 3D Schrödinger equation (10). The 3-D Schrödinger equation is solved directly using the Dirichlet and von Neumann boundary conditions by interpolating wavelet method, and the exact value of surface potential is obtained. The drain current can be estimated by numerically integrating the Equation (23) using Simpson's one-third rule, and the subthreshold values are estimated using Equation (24). The results obtained are validated with experimental values.

Algorithm:

1. Assign gate length, channel length, device width, height and thickness of silicon.
2. Apply bias voltages.
3. Determine numerically the surface potential by solving the 3D Poisson's equation using boundary conditions.
4. Substitute this surface potential value in the 3D Schrödinger's equation.
5. Solve 3-D Schrödinger's equation numerically using Dirichlet and von Neumann boundary conditions.
6. Estimate the exact value of surface potential at every point along the channel length.
7. Obtain subthreshold swing, threshold voltage roll-off, drain characteristics.

5. RESULTS AND DISCUSSION

Numerical computation has been carried out for the nanoscale FinFET. The parameters used for the calculation are given in Table 1.

Figure 2 shows the potential profile of the FinFET photodetector including QM effects obtained using interpolating wavelet method on a grid of $20 \times 13 \times 10$ points. The surface potential $U(x, y, z)$ is calculated for different values of x and constant values of y and z. The figure also

Table 1. Parameters and constants.

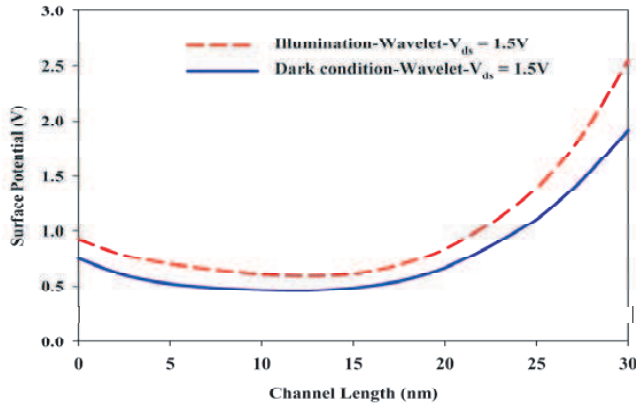| Parameter	Value
Gate Length (L_g)	30 nm
Top gate oxide thickness (T_{ox1})	5 nm
Front (or) back gate thickness (T_{ox2})	1 nm
Channel Length (L_{eff})	30 nm
Thermal Voltage (V_T)	0.025852 V
Intrinsic carrier concentration (n_i)	$9.65 \times 10^9/\mathrm{cm}^3$
Acceptor concentration (N_a)	$1 \times 10^{16}/\mathrm{cm}^3$
Flatband voltage (V_{fb})	-0.48 V
Built-in potential (V_{bi})	0.6 V
Gate voltage (V_g)	0.2 V

Figure 2. Three dimensional potential variation along the channel length under dark and illuminated conditions. $V_g = 0.2$ V, $H_{fin} = 50$ nm, $T_{fin} = 20$ nm and $L_{eff} = 30$ nm, $P_{opt} = 0.5$ W/m^2.

shows the dark condition results including quantum mechanical effects using the same wavelet method for $V_{DS} = 1.5$ V. The surface potential values under illuminated conditions are calculated for $P_{opt} = 0.5$ W/m^2 and $V_{DS} = 1.5$ V. It is found that the surface potential increases with illumination. This is due to the fact that excess carriers generated due to illumination increases the conductivity of the channel. Fig. 3 shows the comparison of surface potential values obtained using interpolating wavelets with WKB approximation values along the channel length
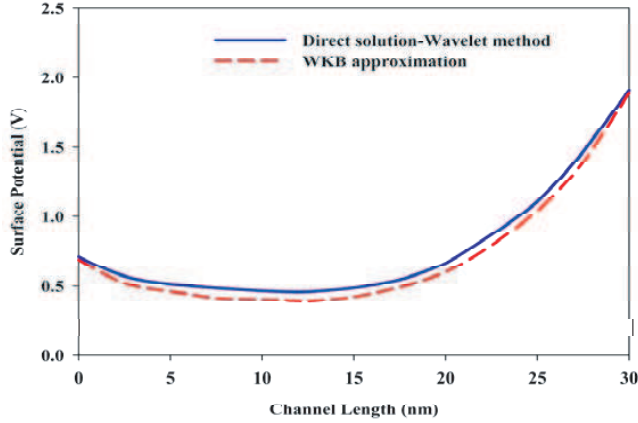
Figure 3. Comparison of surface potential for various methods for $V_{DS} = 1.5\,\mathrm{V}$, $V_g = 0.2\,\mathrm{V}$, $H_{fin} = 50\,\mathrm{nm}$, $T_{fin} = 20\,\mathrm{nm}$ under dark condition.
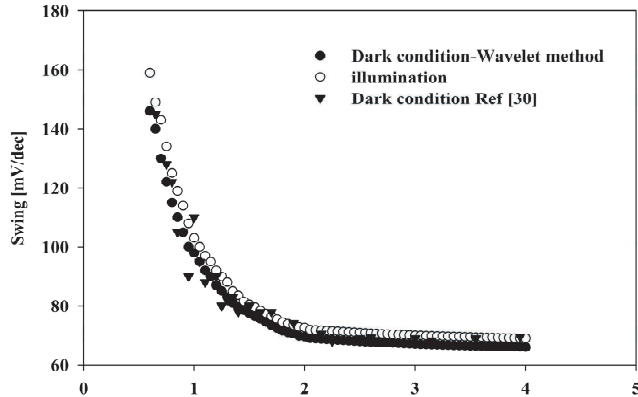

Figure 4. Subthreshold swing of n-channel FinFET photodetector in terms of L_{eff}/T_{eff} for $L_g = 30\,\mathrm{nm}$ and $V_{DS} = 0.1\,\mathrm{V}$, $P_{opt} = 0.5\,\mathrm{W/m}^2$.

including quantum mechanical effects for $V_{ds} = 1.5\,\mathrm{V}$ under dark conditions. It is found that the interpolating wavelet method provides more accurate results than the WKB approximation because the WKB approximation underestimates the density of electrons penetrating into the channel under the potential barrier $U(x, y, z)$ [50]. The S-factor, which is a measure of the subthreshold behavior of the device, is
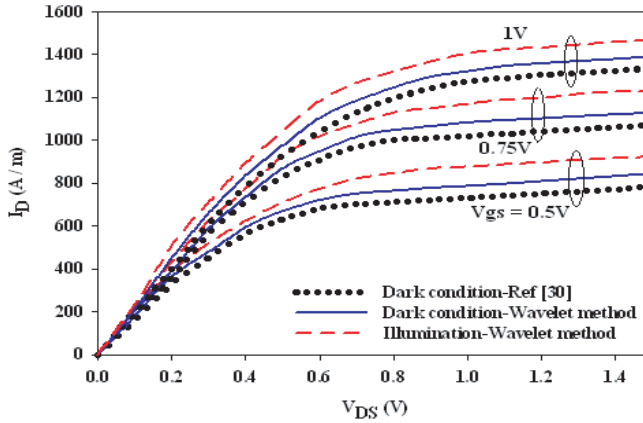
Figure 5. Drain current characteristics of FinFET for various V_{gs} values and $P_{opt} = 0.5$ W/m^2. Dark condition results compared with experimental values [30].

extracted from the $I_{ds} - V_{gs}$ characteristics of the FinFET device. Fig. 4 shows the subthreshold swing for nanoscale FinFET, as a function of L_{eff}/T_{eff} in comparison with the experimental results. The simulation results at $V_{ds} = 0.1$ V exhibit an excellent agreement under dark conditions with the experimental results [30] and validate our model. The dark condition results agree well with experimental results [30]. It is also found that the subthreshold swing increases with illumination. Fig. 5 shows the comparison of $I_D - V_D$ characteristics of nanoscale FinFET at $L_g = 30$ nm and $T_{fin} = 20$ nm for $H_{fin} = 50$ nm. The simulated results under dark condition were compared with experimental ones [30] to validate our model. The values obtained under dark condition using wavelet method shows good agreement with the experimental values. It is also found that the subthreshold leakage current is well suppressed in spite of low channel doping concentration $(1 \times 10^{16}/\text{cm}^3)$. Also, there seems to be no kink effect, which comes from the effect of a floating body. It is shown that for the applied gate-to-source voltage, the drain current also significantly increases. The channel width is determined by applied gate-to-source voltages. The charge carriers pass through the channel, and hence the conduction takes place. When the drain voltage is further increased, more charge carriers try to pass through the channel, resulting in an increase in drain current. But these charge carriers passes through the channel width that is created earlier. Hence the drain current saturates after a

certain limit even if the drain voltage is increased further. The drain current under illuminated condition is higher than dark condition due to generation of excess carriers under illumination. Figs. 6 and 7 show the comparison of $I_d - V_{gs}$ characteristics for a nanoscale FinFET with $L_g = 30$ nm, $T_{fin} = 20$ nm and $V_{ds} = 1.5$ V and 0.1 V. Under dark conditions, the simulated results show a good agreement with experimental ones [30] and validate our model. The drain current values increase under illuminated conditions.
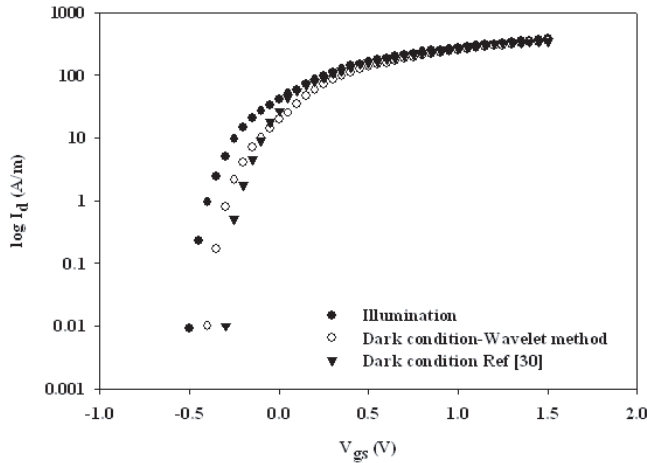

Figure 6. $I_d - V_{gs}$ curves for a n-channel FinFET with $L_g = 30$ nm, $T_{fin} = 20$ nm, $V_{DS} = 1.5$ V, $P_{opt} = 0.5$ W/m^2. Dark condition results compared with experimental values [30].

Table 2. Comparisons of the simulation times & mean relative errors of FDM & Wavelet method for different meshes.

No. of grid points in x, y, z	Simulation Time wavelet (sec)	Mean rel. error Wavelet	Simulation Time FDM (sec)	Mean rel. error FDM
$20 \times 13 \times 10$	109	0.0195	116	0.2158
$45 \times 32 \times 23$	682	0.0075	712	0.1635
$60 \times 49 \times 34$	1646	0.0043	1824	0.0674

Tables 2 and 3 show that different mesh grid points are used in the transport direction for the resolution of Poisson-Schrödinger
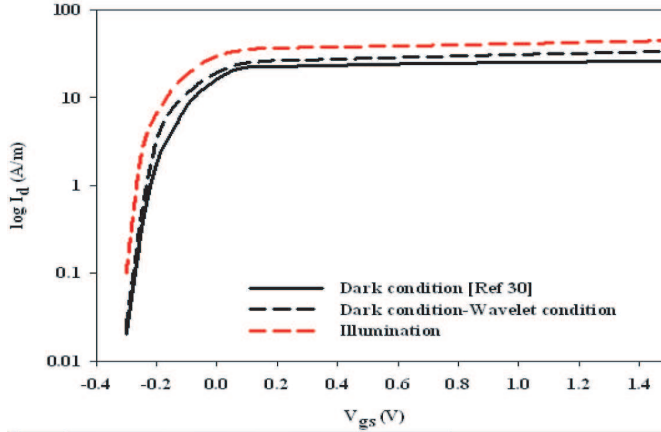
Figure 7. $I_d - V_{gs}$ curves for a n-channel FinFET with $L_g = 30\,\text{nm}$, $T_{fin} = 20\,\text{nm}$, $V_{DS} = 0.1\,\text{V}$, $P_{opt} = 0.5\,\text{W/m}^2$. Dark condition results compared with experimental values [30].

Table 3. Comparisons of the simulation times & mean relative errors of FEM & Wavelet method for different meshes.

No. of grid points in x, y, z	Simulation Time wavelet (sec)	Mean rel. error Wavelet	Simulation Time FEM (sec)	Mean rel. error FEM
$20 \times 13 \times 10$	109	0.0195	245	0.0958
$45 \times 32 \times 23$	682	0.0075	1567	0.0135
$60 \times 49 \times 34$	1646	0.0043	4757	0.0077

equation in order to compute accurate solution. For a $20 \times 13 \times 10$ mesh the wavelet method is compared with experimental results under dark condition for $V_{ds} = 1.5\,\text{V}$. It is found that interpolation method is more accurate than the FDM and FEM methods with considerable reduction in simulation time. The Poisson-Schrödinger equations are solved on the coarser grid. Then the results for the finer grids are interpolated from the coarse ones. This multi-grid procedure enables to use the advantages of interpolating wavelets for obtaining better solution of the coupled Poisson-Schrödinger equation with reduction in simulation time. It is found that the simulation time and relative error reduce considerably with the interpolating wavelet method.

6. CONCLUSION

The wavelet method for modeling nanoscale FinFET photodetector including quantum mechanical effects (QME) shows that the FinFET may retain performance acceptable for OEIC receiver applications even if the gate length is reduced to nanoscale dimension. It also shows the increase in efficiency of the wavelet method as compared to WKB approximation method and FDM and FEM methods. Accurate results have been obtained with significantly reduced computational time. The present work is confined to modeling and simulation of a uniformly doped FinFET. In the future work, three dimensional modeling of non-uniformly doped FinFET including quantum mechanical effects could be carried out. The detailed analysis of noise characteristics can also be obtained, and equivalent circuit model could be developed for accurate characteristics of the device.

REFERENCES

1. Chakrabarti, P., S. Kumar, P. K. Rout, and B. G. Rappai, "A proposed MISFET photodetector," *Proceeding 3rd Asia Pacific Microwave Conference*, 575–578, Tokyo, Japan, 1990.

2. Chakrabarti, P. and I. Venugopal, "Charge-sheet model of a proposed MISFET photodetector," *Phys. Stat. Sol. (A)*, Vol. 147, 277–291, 1995.

3. Ohata, K., "InP MISFET," *Workshop Digest, Asia Pacific Microwave Conference, Tokyo*, 15–20, Japan, 1990.

4. Chakrabarti, P., B. K. Mishra, Y. PratapReddy, and S. Prakash, "Optically controlled characteristics of an InGaAs MISFET," *Phys. Stat. Sol. (A)*, Vol. 147, 277–291, 1995.

5. Okamoto, K. and S. Inoue, "Photoresponse of MOSFET," *Solid-state Electronics*, Vol. 16, 657–662, 1973.

6. Kabeer, M., K. Gowri, and V. Rajamani, "Three dimensional modeling and simulation of a nano MISFET photodetector," *Journal of Optoelectronics and Advanced Materials*, Vol. 9, No. 9, 2879–2885, 2007.

7. Colinge, J.-P., "Multiple-gate SOI MOSFETs," *Solid State Electron.*, Vol. 48, No. 6, 897–905, 2004.

8. Taur, Y., L. H. Wann, and D. J. Frank, "25 nm CMOS design considerations," *IEDM Tech. Dig.*, 789–792, 1998.

9. Taur, Y., D. A. Buchanan, W. Chen, D. J. Frank, K. E. Ismail, S.-H. Lo, G. A. Sai-Halasz, R. G. Viswanathan, H.-J. C. Wann,

S. J. Wind, and H.-S. P. Wong, "CMOS scaling into the nanometer regime," *Proc. IEEE*, Vol. 85, No. 4, 486–504, 1997.

10. Frank, D. J., R. H. Dennard, and E. Nowak, "Device scaling limits of Si MOSFETs and their application dependencies," *Proc. IEEE*, Vol. 89, No. 3, 259–288, 2001.

11. Taur, Y., "CMOS scaling beyond 0.1 μm: How far can it go?" *Proc. Symp. VLSI Technology*, 6–9, 1999.

12. Frank, D. J., S. E. Laux, and M. V. Fischetti, "Monte Carlo simulation of 30 nm dual-gate MOSFET: How short can Si go?," *IEDM Tech. Dig.*, 553–556, 1992.

13. Frank, D. J., S. E. Laux, and M. V. Fischetti, "Monte Carlo simulation of p-and n-channel dual-gate Si MOSFETs at the limits of scaling," *IEEE Trans. Electron Devices*, Vol. 40, 2103, 1993.

14. Yan, R.-H., A. Ourmazd, and K. F. Lee, "Scaling the Si MOSFET: From bulk to SOI to bulk," *IEEE Trans. Electron Devices*, Vol. 39, 1704–1710, 1992.

15. Suzuki, K., T. Tanaka, Y. Tasaka, H. Horie, and Y. Arimato, "Scaling theory for double-gate SOI MOSFETs," *IEEE Trans. Electron Devices*, Vol. 40, 2326–2329, 1993.

16. Wong, H.-S. P., D. J. Frank, Y. Taur, and J. M. C. Stork, "Design and performance considerations for sub-0.1 μm double-gate SOI MOSFETs," *IEDM Tech. Dig.*, 747–750, 1994.

17. Wong, H.-S. P., K. K. Chan, and Y. Taur, "Self-aligned (top and bottom) double-gate MOSFET with a 25 nm thick silicon channel," *IEDM Tech. Dig.*, 427–430, 1997.

18. Lee, J.-H., G. Taraschi, A. Wei, T. A. Langdo, E. A. Fitzgerald, and D. A. Antoniadis, "Super self-aligned double-gate (SSDG) MOSFETs utilizing oxidation rate difference and selective epitaxy," *IEDM Tech., Dig.*, 71–74, 1999.

19. Su, T., J. P. Denton, and G. W. Neudeck, "New planar self-aligned double-gate fully depleted P-MOSFETs using epitaxial lateral overgrowth (ELO) and selectively grown source/drain (S/D)," *IEEE Int. SOI Conf.*, 110–111, 2000.

20. Hisamoto, D., W.-C. Lee, J. Kedzierski, H. Taeuchi, K. Asano, C. Kuo, R. Anderson, T.-J. King, J. Bokor, and C. Hu, "FinFET a self-aligned double-gate MOSFET scalable to 20 nm," *IEEE Trans. Electron Devices*, Vol. 47, 2320–2325, 2000.

21. Huang, X., W.-C. Lee, C. Ion Kuo, D. Hisamoto, L. Chang, J. Kedzierski, R. Anderson, H. Takeuchi, Y.-K. Choi, K. Asano, V. Subramanian, V. King, J. Bokor, and V. Hu, "Sub-50 nm P-channel FinFET," *IEEE Trans. Electron Devices*, Vol. 48, 880–

886, 2001.

22. Dnyanesh Havaldar, S., G. Katti, N. DasGupta, and A. DasGupta, "Subthreshold current model of FinFETs based on analytical solution of 3-D Poisson's Equation," *IEEE Trans. Electron Devices*, Vol. 53, No. 4, 737–742, 2006.

23. Pei, G., J. Kedzierski, P. Oldiges, M. Ieong, V. Chin-Chaun Kan, "FinFET design considerations based on 3-D simulation and analytical modeling," *IEEE Trans. Electron Devices*, Vol. 49, No. 8, 1411–1419, 2002.

24. El Hamid, H. A., J. R. Guitart, V. Kilchytska, D. Flandre, B. Iniguez, "A 3-D analytical physically based model for the subthreshold swing in undoped trigate FinFETs," *IEEE Trans. Electron Devices*, Vol. 54, No. 9, 2487–2496, 2007.

25. Yang, W., Z. Yu, and L. Tian, "Scaling theory for FinFETs based on 3-D effects investigation," *IEEE Trans. Electron Devices*, Vol. 54, No. 5, 1140–1147, 2007.

26. Shao, X. and Z. P. Yu, "Nanoscale FinFET simulation: A quasi-3D quantum mechanical model using NEGF," *Solid-state Electronics*, Vol. 49, 1435–1445, 2005.

27. Lundstrom, M. and J.-H. Rhew, "A landauer approach to nanoscale MOSFETs," *Journal of Computational Electronics*, Vol. 1, 481–489, 2005.

28. Zhang, D., X. Shao, V. Yu, and V. Tiang, "A 3D charge model for FinFET with ballistic transport," *Proc. SISPAD*, 195–198, 2005.

29. Khan, H., V. Mamaluy, and V. Vasileska, "Ballistic quantum-mechanical simulation of 10 nm FinFET using CBR method," *Journal of Physics: Conf. Series*, Vol. 38, 196–199, 2006.

30. Kedzierski, V., V. Fried, E. J. Nowak, V. Kanarsky, J. H. Rankin, H. Hanafi, W. Natzle, D. Boyd, Y. Zhang, V. Roy, J. Newbury, V. Yu, V. Yang, P. Saunders, C. P. Willets, A. Johnson, S. P. Cole, H. E. Young, N. Carpenter, D. Rakowski, B. A. Rainey, P. E. Coltrell, M. Leong, and H.-S. Philip Wong, "High performance symmetric-gate and CMOS-compatible V_t asymmetric-gate FinFET devices," *IEDM Tech. Dig.*, 437–440, 2001.

31. Tang, S. H., L. Chang, N. Lindert, Y.-K. Choi, W.-C. Lee, X. Huang, and V. Subramanian, "FinFET — A quasiplanar double-gate MOSFET," *Proc. Int. Solid-state Circuits Conf. (ISSCC)*, 118–119, 2001.

32. Fried, D. M., A. P. Johnson, E. J. Nowak, J. H. Rankin, and C. R. Willets, "A sub-40 nm body thickness N-type FinFET,"

Proc. Device Res. Conf., 24–25, 2001.

33. Ben Abdallah, N., M. Mouis, and C. Negulescu, "An accelerated algorithm for 2D simulations of the quantum ballistic transport in nanoscale MOSFETs," *Journal of Computational Physics, 2007*, Vol. 225, 74–99, 2006.

34. Ben Abdallah, N. and O. Pinaud, "Multiscale simulation of transport in an open quantum system: Resonances and WKB interpolation," *Journal of Computational Physics*, Vol. 213, 288–310, 2006.

35. Wang, J., "Device physics and simulation of silicon nanowire transistors," Ph.D. Thesis, Purdue University, 2005.

36. Kim, K., O. Kwon, J. Seo, and T. Won, "Nanoscale device modeling and simulation: Fin Field-Effect Transistor (FinFET)," *Japanese Journal of Applied Physics*, Vol. 43, 3784–3789, 2004.

37. De Marchi, L., F. Franze, and E. Baravelli, "Wavelet-based adaptive mesh generation for device simulation," *Solid-state Electronics*, Vol. 50, 650–659, 2006.

38. Jameson, L., "A wavelet-optimized very high order adaptive grid and order numerical method," *SIAM J. SCI Comput.*, Vol. 19, No. 6, 1980–201, 1998.

39. Fatkulin, I. and J. S. Hesthaven, "Adaptive high-order finite-difference method for nonlinear wave problems," *Scientific Computing Report Series*, 2001.

40. Krumholz, M. and L. P. B. Katehi, "MRTD: New time-domain schemes based on multiresolution analysis," *IEEE Trans. Microwave Theory Tech.*, Vol. 44, 555–571, 1996.

41. Tentzeris, M. and J. Harvey, "Time adaptive time-domain techniques for the design of microwave circuits," *IEEE Microwave Guided Wave Lett.*, Vol. 9, 96–99, 1999.

42. Goasguen, S., "Electromagnetic and semiconductor device simulation using interpolating wavelets," *IEEE Trans. on Microwave Theory and Techniques*, Vol. 49, No. 12, 2258–2265, 2001.

43. Yasser, A., A. Hussein, M. Samir, and El-Ghazaley, "Extending Multiresolution Time-Domain (MRTD) technique to the simulation of high-frequency active devices," *IEEE Trans. on Microwave Theory and Techniques*, Vol. 51, No. 7, 1842–1851, 2003.

44. Toupikov, M. and G. Pan, "On nonlinear modeling of microwave devices using interpolating wavelets," *IEEE Trans. on Microwave Theory and Techniques*, Vol. 48, No. 4, 500–509, 2000.

45. Holmstron, M., "Solving hyperbolic PDE's using interpolating

wavelets," *SIAM J. Sci. Comp.*, Vol. 21, No. 2, 405–420, 1999.

46. Daubechies, I., *Ten Lectures on Wavelets*, Capital City Press, Vermont, 1992.

47. Mallat, S., *A Wavelet Tour of Signal Processing*, Academic Press, New York, 1992.

48. Amaratunga, K. and J. R. Williams, "Wavelet-Galerkin solutions of one-dimensional partial-differential equations," *Int. J. Numer. Methods. Eng.*, Vol. 37, 2705–2716, 1994.

49. Janik, T. and B. Majkusiak, "Analysis of the MOS transistor based on the self-consistent solution to the Schrödinger and poisson equations and on the local mobility model," *IEEE Trans. on Electron Devices*, Vol. 45, 1263–1271, 1998.

50. Walls, T. J., V. A. Sverdlov, and K. K. Likharev, "MOSFETs below 10 nm: Quantum theory," *Physica E*, Vol. 19, 23–27, 2003.